ON REYNOLDS STRESS ANISOTROPY IN COMPRESSIBLE CHANNEL FLOW

Holger Foysi
Fachgebiet Strömungsmechanik
TU München, Boltzmannstr. 15, D-85748 Garching, Germany
holger@flm.mw.tu-muenchen.de

Sutanu Sarkar
Department of Mechanical and Aerospace Engineering
Univ. of California San Diego
9500 Gilman Drive, La Jolla, CA 92093-0411, USA
sarkar@ucsd.edu

Rainer Friedrich
Fachgebiet Strömungsmechanik
TU München, Boltzmannstr. 15, D-85748 Garching, Germany
r.friedrich@flm.mw.tu-muenchen.de

ABSTRACT

Three direct numerical simulations of turbulent supersonic channel flow have been performed for global Mach numbers ranging from 1.5 to 3 and Reynolds numbers based on friction velocity ranging from 221 to 545.

By comparison with incompressible channel data it is shown that compressibility causes structural changes in the Reynolds stresses and those tensors which determine their transport, e.g., the pressure-rate-of-strain tensor. Conclusive explanations are provided for the increase in streamwise Reynolds stress as the Mach number increases, for the decrease in its production rate and the decrease in the pressure-rate-of-strain tensor component. Furthermore, outer scalings are provided for the Reynolds stresses and the pressure-rate-of-strain tensor.

INTRODUCTION

Compressible turbulent channel flow between isothermal walls for global Mach numbers up to $M = 3$ has been first studied by Coleman et al. (1995) using direct numerical simulation and a body force which replaces the mean pressure gradient and is homogeneous in wall-parallel planes. Their results showed that the flow is strongly controlled by wall-normal gradients of mean density and temperature, to the point that most of the density- and temperature fluctuations are a result of solenoidal mixing. Hence, van Driest transformation of the mean velocity and a semi-local near-wall scaling suggested by Huang *et al.* (1995) for r.m.s. velocity and vorticity fluctuations proved to be successfull in collapsing compressible and incompressible data. Further investigations into intrinsic compressibility effects (Huang, 1995) showed that explicit compressibility terms like pressure-dilatation correlations and compressible dissipation rate are negligibly small up to Mach numbers of 3 and that the turbulent kinetic energy and its production rate scale with the wall shear stress, τ_w, and with $\tau_w u_m/h$ (the bulk velocity and channel half width), respectively. Lechner *et al.* (2001) provided more details about the nature of fluctuating variables and structural compressibility effects in compressible isothermal channel flow at $M = 1.5$. They presented budgets for all Reynolds stress components and demonstrated that production, dissipation, diffusion and pressure-strain terms, coincide with the corresponding incompressible terms (Kim, 1989) in the channel core when scaled with $\tau_w u_m/h$. Li *et al.* (2002) addressed compressibility effects in high-speed compressible channel flow between isothermal walls. Following Coleman *et al.* (1995) they used a dynamic energy sink to shut off the heat generated by mean and turbulent dissipation. This leads to uniform mean density and temperature profiles across the channel, thus removing effects due to mean property variation, and revealing the pure role of dilatational fluctuations. For a center-line Mach number of 6.2 they found that the pressure-dilation term reaches 17% of the peak turbulent kinetic energy production. Recently, Morinishi *et al.* (2003) investigated compressible turbulent channel flow using a B-spline collocation method in their DNS. They validated their numerical algorithm against the $M = 1.5$, $Re = 3000$ case of Coleman *et al* (1995) and computed a second flow with the same M, Re parameters, but with one isothermal and one adiabatic wall. This case is of considerable interest, since it shows that the mean velocity normalized by u_τ matches incompressible channel data on the adiabatic wall side without van Driest transformation, while the part of the profile starting from the isothermal wall side matches Coleman *et al.*'s (1995) data and deviates from incompressible data due to mean property variations.

This paper focusses on compressible channel flow between isothermal walls at various Reynolds and Mach numbers. It addresses changes in Reynolds stress anisotropy and in the behaviour of the pressure-rate-of-strain tensor in more detail and provides conclusive explanations for these effects.

DESCRIPTION OF THE NUMERICAL METHOD AND DNS PARAMETERS

The *numerical method* starts from a pressure-velocity-entropy formulation of the compressible Navier-Stokes equations:

$$\frac{\partial p}{\partial t} = -u_j \frac{\partial p}{\partial x_j} - \gamma p \frac{\partial u_j}{\partial x_j} + (\gamma - 1)\left(\Phi - \frac{\partial q_j}{\partial x_j}\right), \tag{1}$$

$$\frac{\partial u_i}{\partial t} = -u_j \frac{\partial u_i}{\partial x_j} - \frac{1}{\rho}\left(\frac{\partial p}{\partial x_i} - \frac{\partial \tau_{ij}}{\partial x_j}\right) + \frac{1}{\rho} f_1 \delta_{i1}, \tag{2}$$

$$\frac{\partial s}{\partial t} = -u_j \frac{\partial s}{\partial x_j} + \frac{R}{p}\left(\Phi - \frac{\partial q_j}{\partial x_j}\right), \tag{3}$$

where p, u_i, s, ρ represent pressure, Cartesian velocity components, entropy and density, respectively. The components of the heat flux

vector $\mathbf{q}$, viscous stress tensor τ and dissipation rate Φ read:

$$q_i = -\lambda \frac{\partial T}{\partial x_i}, \quad \tau_{ij} = 2\mu s_{ij} - \frac{2}{3}\mu s_{kk}\delta_{ij}, \tag{4}$$

$$\Phi = \tau_{ij} s_{ij}, \quad s_{ij} = \frac{1}{2}\left(\frac{\partial u_i}{\partial x_j} + \frac{\partial u_j}{\partial x_i}\right). \tag{5}$$

The thermal equation of state

$$p = \rho R T, \quad R = C_p - C_v, \tag{6}$$

and the following laws for dynamic viscosity μ and heat conductivity λ close the set of equations:

$$\frac{\mu}{\mu_{ref}} = \left(\frac{T}{T_{ref}}\right)^n, \quad \lambda = \mu \frac{C_p}{Pr}, \quad n = 0.7 \tag{7}$$

The Prandtl number Pr and the ratio of specific heats γ are kept at constant values in the temperature range considered, namely $Pr = 0.7$, $\gamma = C_p/C_v = 1.4$. The body force term $f_1\delta_{i1}$ in the momentum equation replaces the mean pressure gradient in streamwise direction and is uniform in 3D space. Thus, fully developed turbulent flow can be handled using periodic boundary conditions in stream- and spanwise directions. Following Sesterhenn (2001) equations (3) are cast in a characteristic non-conservative form which contains 'fluxes' of the form

$$X_i^{\pm} = (u_i \pm c)\left(\frac{1}{\rho c}\frac{\partial p}{\partial x_i} \pm \frac{\partial u_i}{\partial x_i}\right) \quad \text{(no summation!)} \tag{8}$$

in the hyperbolic part of the Navier-Stokes equations, describing transport in positive and negative coordinate directions. Here, $c = \sqrt{\gamma p/\rho}$ is the speed of sound. The advantage of this special form (Sesterhenn, 2001) is that wall boundary conditions can be derived consistently with the equations. At a solid isothermal and stationary wall normal to the x_3-direction, at which

$$\frac{\partial u_i}{\partial t} = \frac{\partial T}{\partial t} = 0, \quad i = 1,2,3 \tag{9}$$

we obtain the boundary conditions:

$$X_3^+ = X_3^- + \frac{2}{\rho}\frac{\partial \tau_{3j}}{\partial x_j} \tag{10}$$

$$\frac{\partial p}{\partial t} = -\frac{p}{2c}(X_3^+ + X_3^-) \tag{11}$$

$$\frac{\partial s}{\partial t} = \frac{R}{2c}(X_3^+ + X_3^-) \tag{12}$$

which show explicitly that p, s evolve in time at the wall. A compact 5th-order upwind scheme of Adams and Shariff (1996) is used to discretize the hyperbolic (Euler) terms in (1-3). The viscous and heat conduction terms are discretized with a compact 6th order scheme of Lele (1992). The solution is advanced in time with a third-order 'low-storage' Runge-Kutta scheme, proposed by Williamson (1980).

Three direct simulations have been performed for different *flow parameters*. The global Mach and Reynolds numbers for fully developed channel flow read

$$M = u_{av}/c_w, \quad Re = \rho_m u_{av} h/\mu_w. \tag{13}$$

The bulk-averaged density ρ_m is defined as $\rho_m = \int_0^h \bar{\rho} dx_3/h$, u_{av} is the Reynolds (rather than Favre) cross-sectionally averaged velocity. The speed of sound and viscosity are computed for constant wall temperature T_w, while h is the channel half width. The friction Reynolds number $Re_\tau = \rho_w u_\tau h/\mu_w$, with $u_\tau = \sqrt{\tau_w/\rho_w}$, is a result of the simulation. Table 1 summarizes the flow parameters, box sizes and numbers of grid points used in the three cases A-C. Equidistant grids are used in (x_1, x_2)-directions. In the wall-normal x_3-direction, points are clustered following tanh-functions (Lechner, 2001). The first gridpoint is below $x_3^+ = 1.5$ and the tenth at $x_3^+ \leq 17.62$ (case C).

Table 1: Flow and computational parameters

Case	M	Re	Re_τ	$\frac{L_{x_1}}{h}$	$\frac{L_{x_2}}{h}$	$\frac{L_{x_3}}{h}$
A	1.5	3000	221	4π	$4\pi/3$	2
B	2.5	5000	455	2π	$2\pi/3$	2
C	3.0	6000	545	2π	$2\pi/3$	2

Table 2: Flow and computational parameters (cont.)

Case	N_{x1}	N_{x2}	N_{x3}	Δx_1^+	Δx_2^+	$\Delta x_{3\,max}^+$
A	192	128	151	14.46	7.23	5.02
B	256	128	201	11.16	7.44	7.46
C	256	128	201	13.37	8.91	9.38

MEAN MOMENTUM TRANSPORT

Compressible channel flow driven by a mean body force $\bar{f}_1\delta_{i1}$ is homogeneous in planes parallel to the walls. For the mean mass fluxes we therefore get:

$$(\bar{\rho}\tilde{u}_1, \bar{\rho}\tilde{u}_2, \bar{\rho}\tilde{u}_3)^T = (\bar{\rho}\tilde{u}_1(x_3), 0, 0)^T. \tag{14}$$

The tilde denotes Favre averaging. The Reynolds averaged wall-normal velocity $\overline{u_3}$, on the other hand, is nonzero and equals the mean Favre fluctuation:

$$\overline{u_3} = \overline{u_3''} = -\overline{\rho' u_3'}/\bar{\rho} \tag{15}$$

The mean momentum balance in streamwise direction reads

$$0 = \frac{\partial}{\partial x_3}(\bar{\tau}_{13} - \overline{\rho u_1'' u_3''}) + \bar{f}_1 \tag{16}$$

Integrating this from the wall to the centre-line ($x_3 = h$) provides the spatially homogeneous body force that replaces the mean pressure gradient:

$$\bar{f}_1 = \frac{\tau_w}{h} = -\frac{\partial \bar{p}}{\partial x_1}. \tag{17}$$

Integrating (16) from the wall to a position x_3 shows that the total shear stress (sum of Reynolds and viscous stress) varies linearly, as in incompressible channel flow. In wall units (ρ_w, μ_w, $u_\tau = \sqrt{\tau_w/\rho_w}$) we get:

$$\frac{\bar{\mu}}{\mu_w}\frac{\partial \overline{u_1}^+}{\partial x_3^+} - \frac{\overline{\rho u_1'' u_3''}}{\tau_w} = 1 - \frac{x_3}{h} \tag{18}$$

where we have neglected correlations involving viscosity fluctuations, since they are small in supersonic flow (Huang, 1995). The mean momentum balance in wall-normal direction is:

$$0 = -\frac{\partial}{\partial x_3}(\bar{p} - \overline{\rho u_3''^2} - \overline{\tau_{33}}) \tag{19}$$

After integration and assuming $\overline{\tau}_{33} \approx 4/3\bar{\mu}\partial\overline{u}_3/\partial x_3$, we obtain in wall units:

$$\frac{\bar{p} - p_w}{\tau_w} = \frac{4}{3}\frac{\bar{\mu}}{\mu_w}\frac{\partial \overline{u_3}^+}{\partial x_3^+} - \frac{\overline{\rho u_3''^2}}{\tau_w} \tag{20}$$

The first term on the r.h.s. is associated with the mean dilatation. It is small everywhere in the channel (Figure 1).

Outer scaling: From (18) it is clear that $\overline{\rho u_1'' u_3''}$ scales with τ_w in the core region where viscous stresses are negligible. Similarly, $\overline{\rho u_3''^2}$ and $(\overline{p} - p_w)$ scale with τ_w there. Figure 1 shows the normalized pressure difference together with profiles of the viscous term in (20) for cases A-C and incompressible channel flow. In all cases does the Reynolds normal stress $\overline{\rho u''^2}$ control the mean pressure variation.

Inner scaling: Huang *et al.* (1995) have suggested semi-local scaling to collapse compressible data onto incompressible ones. We adopt this scaling here and use the local values of $\overline{\rho}$, $\overline{\mu}$ and

$$u_\tau^* = \sqrt{\tau_w/\overline{\rho}} = u_\tau \sqrt{\rho_w/\overline{\rho}}. \tag{21}$$

The non-dimensional wall-normal coordinate then is $x_3^* = \overline{\rho} u_\tau^* x_3/\overline{\mu}$. As demonstrated in Figure 2, the non-dimensional pressure difference, $(\overline{p} - p_w)/\tau_w$ and hence $\overline{\rho u_3''^2}/\tau_w$ collapse much better for different Mach numbers in the wall layer when plotted against x_3^*. While the van Driest transformed velocity, $\tilde{u}_{1,VD}^+ = \int_0^{\tilde{u}_1^+} \sqrt{\overline{\rho}/\rho_w}\, d\tilde{u}_1^+$, plotted against x_3^+ collapses the profiles in the log-layer, it is a viscosity-transformed velocity, $u_{1,\nu}^+ = \int_0^{\tilde{u}_1^+} \overline{\mu}/\mu_w\, d\tilde{u}_1^+$, which makes the profiles coincide in the sublayer (Figure 3).

REYNOLDS STRESSES AND THEIR TRANSPORT

From the momentum balance (18) and the fact that the correlation coefficient of $\overline{\rho u_1'' u_3''}$ is practically independent of Mach number (Coleman, 1995), we conclude that $\overline{\rho u_1''^2}$ and $\overline{\rho u_3''^2}$, finally all Reynolds stresses scale with τ_w in the channel core. Figure 4 contains profiles of $\overline{\rho u_1''^2}$ for three incompressible and three compressible cases as an example to show that the outer scaling applies for $x_3/h > 0.4$.

An explanation for, why $\overline{\rho u_1''^2}/\tau_w$ in the case of compressible flow overshoots the corresponding incompressible values in the buffer region has to start from its transport equation, viz:

$$\begin{aligned} 0 = \quad & -\overline{\rho u_1'' u_3''} \frac{\partial \tilde{u}_1}{\partial x_3} - \frac{\partial}{\partial x_3}\left(\overline{\rho u_2'' u_3''}/2 - \overline{u_1' \tau_{13}}\right) + \\ & \overline{u_1''}\left(\frac{\partial \overline{\tau_{13}}}{\partial x_3} - \frac{\partial \overline{p}}{\partial x_1}\right) + \overline{p' \frac{\partial u_1'}{\partial x_1}} - \overline{\tau_{1j} \frac{\partial u_1'}{\partial x_j}}. \end{aligned} \tag{22}$$

The terms describe production P_{11}, turbulent and viscous diffusion TD_{11}, VD_{11}, mass flux variation M_{11}, pressure- rate-of-strain correlation Π_{11} and turbulent dissipation DS_{11}. Since the 'pressure-diffusion' term drops out, Π_{11} equals the velocity-pressure-gradient term VPG_{11}. The balance (22) normalized by $\tau_w u_{av}/h$ is shown in Figure 5 for one incompressible and the compressible case C. Here, u_{av} is the bulk velocity defined by $u_{av} = \int_0^1 \overline{u_1} d(x_3/h)$. The production terms peak in the buffer layer ($x_3^+ < 30$). Compressibility reduces the production rate and at the same time reduces turbulent dissipation, turbulent transport and redistribution (Π_{11}). The reduction of the latter three terms together is greater than the reduction of P_{11}. This is why the level of $\overline{\rho u_1''^2}/\tau_w$ is higher in compressible channel flow with isothermal walls.

The reduction in the production rate will be explained now. We compute the spatial extremum of P_{11} via:

$$\frac{d}{dx_3^+}\left(-\frac{\overline{\rho u_1'' u_3''}}{\tau_w}\frac{d\tilde{u}_1^+}{dx_3^+}\right) \simeq \frac{d}{dx_3^+}\left(-\frac{\overline{\rho u_1'' u_3''}}{\tau_w}\frac{d\overline{u_1}^+}{dx_3^+}\right) = 0 \tag{23}$$

For high Reynolds numbers the Reynolds shear stress satisfies in the buffer layer the simplified relation (18):

$$-\frac{\overline{\rho u_1'' u_3''}}{\tau_w} = 1 - \frac{\overline{\mu}}{\mu_w}\frac{d\overline{u_1}^+}{dx_3^+}. \tag{24}$$

Using this in (23) and differentiating, we get:

$$\frac{\overline{\mu}}{\mu_w}\frac{d\overline{u_1}^+}{dx_3^+} = \frac{1}{2}\left(1 - \left(\frac{d\overline{u_1}^+}{dx_3^+}\right)^2 \frac{d\overline{\mu}/\mu_w}{dx_3^+} \Big/ \frac{d^2\overline{u_1}^+}{dx_3^{+2}}\right) \tag{25}$$

For channel flow between cooled walls the term in the bracket adds to a quantity larger than 1, since $d(\overline{\mu}/\mu_w)/dx_1^+ > 0$ and $d^2\overline{u_1}^+/dx_3^{+2} < 0$. Hence,

$$\frac{\overline{\mu}}{\mu_w}\frac{d\overline{u_1}^+}{dx_3^+} > \frac{1}{2} \tag{26}$$

and, from (24), it follows that

$$-\frac{\overline{\rho u_1'' u_3''}}{\tau_w} < \frac{1}{2}. \tag{27}$$

The corresponding relations for incompressible channel flow are that, at the point of maximum production P_{11},

$$\frac{d\overline{u_1}^+}{dx_3^+} = \frac{1}{2}, \quad -\frac{\overline{u_1' u_3'}}{u_\tau^2} = \frac{1}{2}. \tag{28}$$

In compressible channel flow between cooled walls, the Reynolds shear stress and the peak production of $\overline{\rho u_1''^2}$ and $\overline{\rho} k$ are therefore reduced with respect to incompressible isothermal flow as a result of viscous heating. The upper bound ($Re_\tau \to \infty$) for the peak production rate is:

$$\left(-\frac{\overline{\rho u_1'' u_3''}}{\tau_w}\frac{d\overline{u_1}^+}{dx_3^+}\right)_{Re_\tau \to \infty} < \frac{1}{4} \tag{29}$$

REYNOLDS STRESS ANISOTROPY

The Reynolds stress anisotropy tensor is defined by

$$b_{ij} = \frac{\overline{\rho u_i'' u_j''}}{\overline{\rho u_k'' u_k''}} - \frac{1}{3}\delta_{ij}. \tag{30}$$

In order to show how its four components are affected by compressibility, we concentrate on two flow cases, namely incompressible channel flow at $Re_\tau = 590$ and compressible channel flow at $Ma = 3$, $Re_\tau = 545$, see Figure 6. The compressibility effects we observe in the channel are in agreement with corresponding effects in homogeneous shear flow (Sarkar, 1995), namely an increase in all normal stress anisotropies and a decrease in the shear stress anisotropy with increasing Mach number. The state of b_{ij} is well characterized by its two invariants II, III. Figure 7 shows Lumley's triangle and the turbulence state for case C only, for clarity. There is hardly any difference to the incompressible case (not shown). Near the wall the turbulence state is two-dimensional. At around $x_3^+ = 16$ it is closest to 1D and then approaches a nearly isotropic state in the core region. The cross marks a case of incompressible homogeneous shear flow (Ristorcelli, 1995).

PRESSURE-RATE-OF-STRAIN TENSOR

An important issue concerning turbulence modeling is the reduction of terms involving pressure fluctuations, like the redistribution Π_{ij} and velocity-pressure-gradient term (VPG_{ij}). Figures 8 and 10 to 12 contain profiles of Π_{ij} normalized with $\tau_w u_{av}/h$ and plotted against x_3/h for cases A-C and the same incompressible cases used in Figure 4. The collapse of curves in the channel core is striking. At the same time there are strong effects of Reynolds and Mach number in the wall layer.

Outer scaling: $\tau_w u_{av}/h$ can be shown to be the proper outer scale of all components of the pressure-rate-of-strain tensor $\Pi_{ij} = \overline{p'(u_{i,j}' + u_{j,i}')}$. Its trace is non-zero, but small compared to the solenoidal dissipation rate of $\overline{\rho} k$ (TKE) and it increases with Mach number (Huang, 1995). The outer scaling of Π_{ij},

$$\Pi_{ij} = (\tau_w/h) u_{av} f_{ij}(x_3/h) \tag{31}$$

is obtained by first noticing, from the Reynolds normal stress transport equations, that Π_{ij} and $\varepsilon_{ij} \approx 2/3\overline{\rho}\varepsilon\delta_{ij}$ are of the same order (see Figure 5) when $y/h > 0.2$, and then estimating the dissipation rate of k as follows. The mean total enthalpy equation integrated across the half channel relates the wall heat flux q_w to the pressure work done in the channel:

$$q_w = -\tau_w u_{av} \tag{32}$$

Similarly, the integrated mean internal energy equation provides

$$q_w \simeq \int_0^h \left(\overline{\mu} \left(\frac{d\overline{u_1}}{dx_3} \right)^2 + \overline{\rho}\varepsilon \right) dx_3 \tag{33}$$

The contribution by the pressure-dilatation correlation, $\overline{p' u'_{i,i}}$, has been neglected. An estimation of the direct dissipation part in (33) is obtained using partial integration:

$$\int_0^h \overline{\mu} \left(\frac{d\overline{u_1}}{dx_3} \right)^2 dx_3 = \left(\overline{u_1} \overline{\mu} \frac{d\overline{u_1}}{dx_3} \right) \Big|_0^h - \int_0^h \overline{u_1} \frac{d}{dx_3} \left(\overline{\mu} \frac{d\overline{u_1}}{dx_3} \right) dx_3 \simeq u_{av}\tau_w \tag{34}$$

Combining relations (32) - (34) therefore implies that, in the outer layer,

$$\overline{\rho}\varepsilon = (\tau_w/h) u_{av} f_\varepsilon(x_3/h), \tag{35}$$

consistent with (31).

Inner scaling: As shown in Figure 8, the magnitude of Π_{11} and similarly that of Π_{22} and Π_{33} (Figures 10,11) is reduced in the wall layer, when the flow is compressible. Π_{13}, presented in Figure 12, partly follows that trend as well. If we assume an inner scaling for Π_{ij} in the case of incompressible flow of

$$(\Pi_{ij})_{inc} = \frac{\tau_w u_\tau^2}{\nu} f_{ij}(x_3^+) = \frac{\tau_w^2}{\mu} f_{ij}(x_3^+) \tag{36}$$

and suppose that this scaling holds for compressible flow with x_3^+ replaced by $x_3^* = x_3 \overline{\rho} u_\tau^* / \overline{\mu}$ and μ replaced by $\overline{\mu}$, then the following relation explains the observed reduction in Π_{ij} in the inner layer:

$$\Pi_{ij} / \left(\frac{\tau_w u_{av}}{h} \right) = Re_\tau \frac{u_\tau}{u_{av}} \frac{\mu_w}{\overline{\mu}} g_{ij}(x_3^*). \tag{37}$$

For the same Reynolds number, the reduction in Π_{ij} is partly due to the well-known decrease in u_τ/u_{av} (i.e. skin friction) with increasing Mach number, and partly due to viscosity variation. Figure 9 presents Π_{11} normalized by $\tau_w^2/\overline{\mu}$ as a function of x_3^* for the same cases as in Figure 8. The large differences in Π_{11} due to M and Re_τ in the wall layer seen in Figure 8 are now clearly reduced by this scaling.

CONCLUDING REMARKS

DNS data of compressible and incompressible channel flow have been used to analyse changes in Reynolds stress anisotropy and in the behaviour of the pressure-rate-of-strain tensor.

Explanations have been given for the reduction in Reynolds shear stress, peak TKE production rate and pressure-rate-of-strain tensor components with increasing Mach number. Conclusive outer-scaling laws are presented.

A better understanding of the behaviour of pressure fluctuations in compressible channel flow is still needed based on an analysis of the pressure Poisson equation in order to unravel the role of density fluctuations in the channel core and of the mean density gradient in the wall layer.

REFERENCES

H. Abe, H. Kawamura, H. Choi: "The Reynolds-number dependence of the wall shear-stress and pressure fluctuations in a turbulent channel flow". Proc. 7th TRA Conference, Turbulence Research Association, April 2002, Seoul National University, pp. 103-114.

N.A. Adams, K. Shariff: "A high-resolution hybrid compact-ENO scheme for shock-turbulence interaction problems". JCP **127**, 1996, pp. 27

G.N. Coleman, J. Kim, R.D. Moser: "Turbulent supersonic isothermal-wall channel flow". J. Fluid Mech. **305**, 1995, pp. 159-183

P.G. Huang, G.N. Coleman, P. Bradshaw: "Compressible turbulent channel flows: DNS results and modelling". J. Fluid Mech. **305**, 1995, pp. 185-218

J. Kim, P. Moin, R.D. Moser:"Turbulence statistics in fully developed channel flow at low Reynolds number". J. Fluid Mech. **177**, 1987, pp. 133

J. Kim: "On the structure of pressure fluctuations in simulated turbulent channel flow". J. Fluid Mech. **205**, 1989, pp. 421-451

R. Lechner, J. Sesterhenn, R. Friedrich: "Turbulent supersonic channel flow". J. Turbulence **2**, 2001, pp. 1-25

S. Lele: "Compact Finite Difference Schemes with Spectral-like Resolution". J. Comp. Phys. **103**, 1992, pp. 16-42

Q. Li, N.D. Sandham, G.N. Coleman:"DNS of high-speed compressible channel flows". *Advances in Turbulence IX*, 2002, pp. 359

Y. Morinishi, S. Tamano, K. Nakabayashi: "A DNS algorithm using B-spline collocation method for compressible turbulent channel flow". Computers & Fluids **32**, 2003, pp. 751-776

R.D. Moser, J. Kim, N.N. Mansour: "Direct numerical simulation of turbulent channel flow up to $Re_\tau = 590$". Phys. Fluids **11**, 1999, pp. 943-945

J.R. Ristorcelli: "Diagnostic Statistics for the Assessment and Characterization of Complex Turbulent Fows". ICASE Report No. 95-67; also, NASA CR 198221, December 1995

S. Sarkar: "The stabilizing effect of compressibility in turbulent shear flow". J. Fluid Mech. **282**, 1995, pp. 163-186

J. Sesterhenn: "A characteristic-type formulation of the Navier–Stokes equations for high order upwind schemes". Computers & Fluids **30**, 2001, pp. 37

J.H. Williamson: "Low-storage Runge-Kutta schemes", J. Comp. Physics **35**, 1980, pp. 48-56

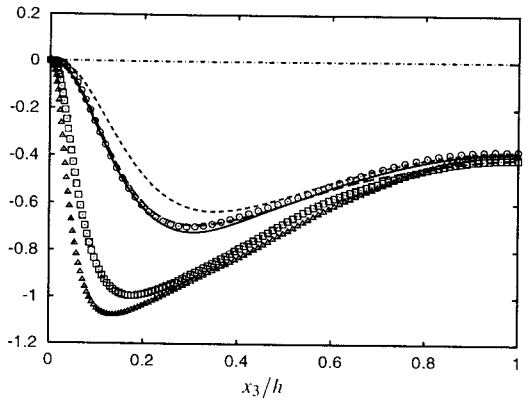

Figure 1: $(\overline{p}-p_w)/\tau_w$, is plotted as a function of x_3/h. Compressible cases: ——, $Re_\tau = 545$, $Ma = 3$; – – –, $Re_\tau = 455$, $Ma = 2.5$;- - - -, $Re_\tau = 221$, $Ma = 1.5$; · · · ·, $\frac{4}{3}\frac{\overline{\mu}}{\mu_w}\frac{\partial \overline{u_1}^+}{\partial x_3^+}$ for $Re_\tau = 545$, $Ma = 3$. Incompressible cases (Moser, 1999) : △ $Re_\tau = 590$; □ $Re_\tau = 395$; ⊙ $Re_\tau = 180$.

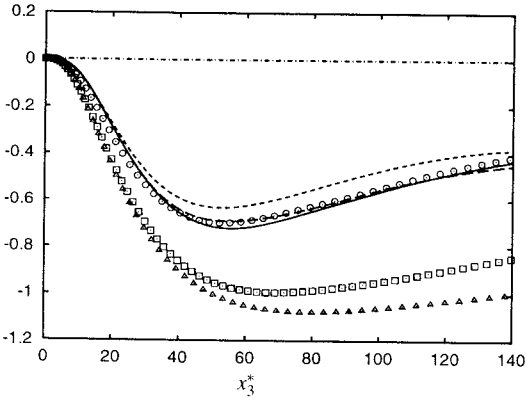

Figure 2: $(\overline{p}-p_w)/\tau_w$, is plotted as a function of x_3^*. Compressible cases: ——, $Re_\tau = 545$, $Ma = 3$; – – –, $Re_\tau = 455$, $Ma = 2.5$;- - - -, $Re_\tau = 221$, $Ma = 1.5$; · · · ·, $\frac{4}{3}\frac{\overline{\mu}}{\mu_w}\frac{\partial \overline{u_1}^+}{\partial x_3^+}$ for $Re_\tau = 545$, $Ma = 3$. Incompressible cases (Moser, 1999) : △ $Re_\tau = 590$; □ $Re_\tau = 395$; ⊙ $Re_\tau = 180$.

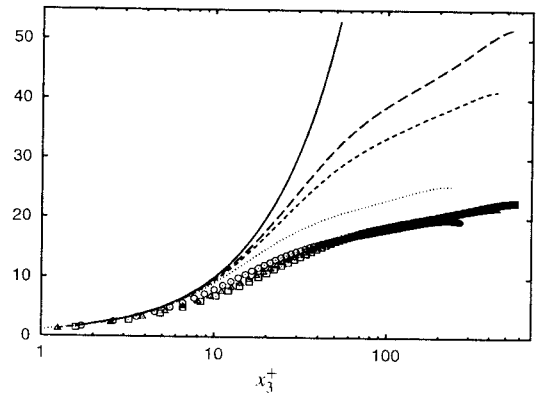

Figure 3: Profiles of $\int_0^{\overline{u_1}^+} \overline{\mu}/\mu_w d\overline{u_1}^+$ (lines) and the Van Driest transformed velocity (symbols) ——, x_3^+; – – –, □ $Re_\tau = 545$, $Ma = 3$; - - - -, △, $Re_\tau = 455$, $Ma = 2.5$; · · · · · ·, ⊙, $Re_\tau = 221$, $Ma = 1.5$

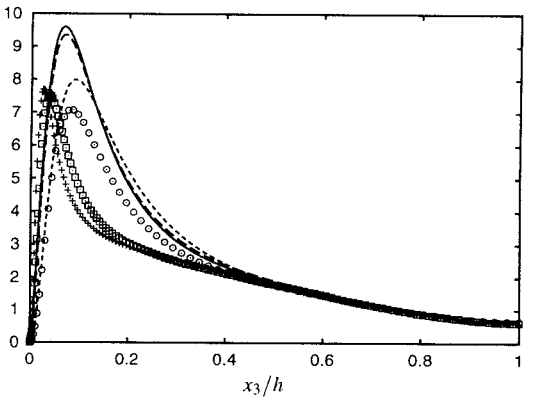

Figure 4: $\overline{\rho u_1''^2}$ normalized by τ_w. *Compressible cases*: ——, $Re_\tau = 545$, $Ma = 3$; – – –, $Re_\tau = 455$, $Ma = 2.5$; - - - -, $Re_\tau = 221$, $Ma = 1.5$. *Incompressible cases* (Moser, 1999): ⊙ $Re_\tau = 180$; □ $Re_\tau = 395$; + $Re_\tau = 590$.

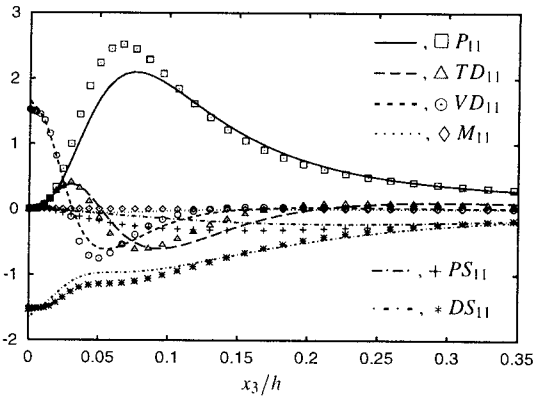

Figure 5: $\overline{\rho u_1''^2}/2$-balance. The lines show case A, the symbols denote the incompressible data of Moser (1999), $Re_\tau = 180$.

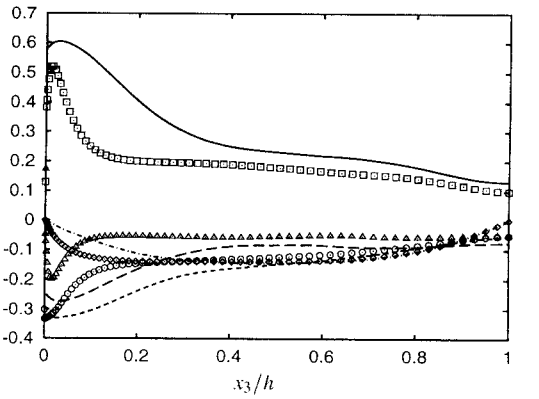

Figure 6: Profiles of all four components of the anisotropy tensor $b_{ij} = \overline{\rho u_i'' u_j''}/\overline{\rho u_k'' u_k''} - 1/3\delta_{ij}$. Case C, $Re_\tau = 545$, $Ma = 3$: ——, b_{11}; – – –, b_{22}; - - - -, b_{33}; -·-·-, b_{13}. $Re_\tau = 590$ (Moser, 1999): □ b_{11}; △ b_{22}; ⊙ b_{33}; ◇ b_{13}.

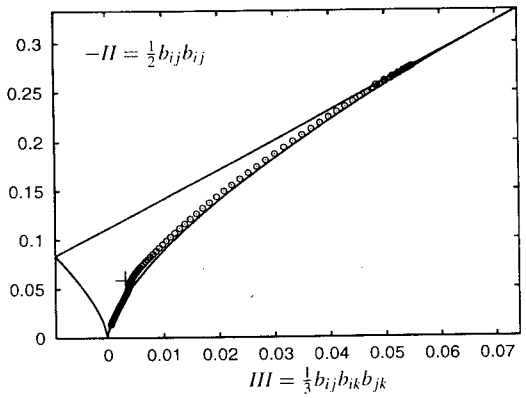

Figure 7: Anisotropy invariant map for $Re_\tau = 545$, $Ma = 3$. +,: homogeneous shear flow (Ristorcelli, 1995)

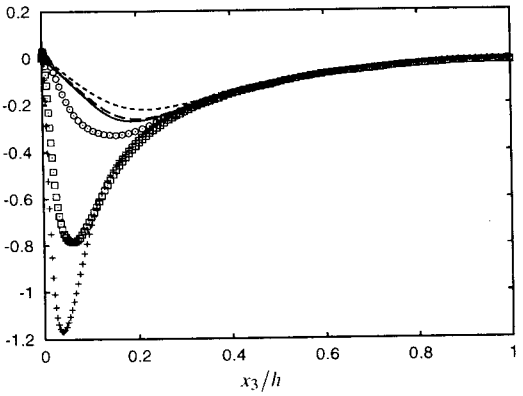

Figure 8: Π_{11} normalized by $\tau_w u_{av}/h$. *Compressible cases*: ——, $Re_\tau = 545$, $Ma = 3$; – – –, $Re_\tau = 455$, $Ma = 2.5$; - - - -, $Re_\tau = 221$, $Ma = 1.5$. *Incompressible cases* (Moser, 1999): ⊙ $Re_\tau = 180$; □ $Re_\tau = 395$; + $Re_\tau = 590$.

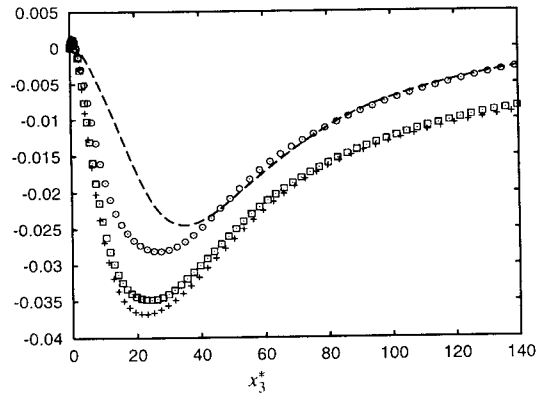

Figure 9: Π_{11} normalized by $\tau_w^2/\bar{\mu}$ using semi- local scaling. *Compressible cases*: ——, $Re_\tau = 545$, $Ma = 3$; – – –, $Re_\tau = 455$, $Ma = 2.5$; - - - -, $Re_\tau = 221$, $Ma = 1.5$. *Incompressible cases* (Moser, 1999): ⊙ $Re_\tau = 180$; □ $Re_\tau = 395$; + $Re_\tau = 590$.

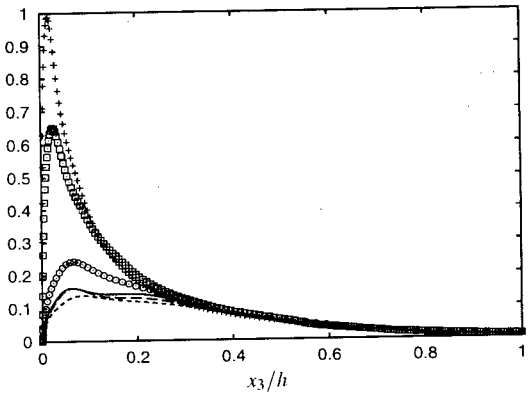

Figure 10: Π_{22} normalized by $u_{av}\tau_w/h$. *Compressible cases*: ——, $Re_\tau = 545$, $Ma = 3$; – – –, $Re_\tau = 455$, $Ma = 2.5$; - - - -, $Re_\tau = 221$, $Ma = 1.5$; · · · · · ·, $Re_\tau = 181$, $Ma = 0.3$. *Incompressible cases* (Moser, 1999): ⊙ $Re_\tau = 180$; □ $Re_\tau = 395$; + $Re_\tau = 590$.

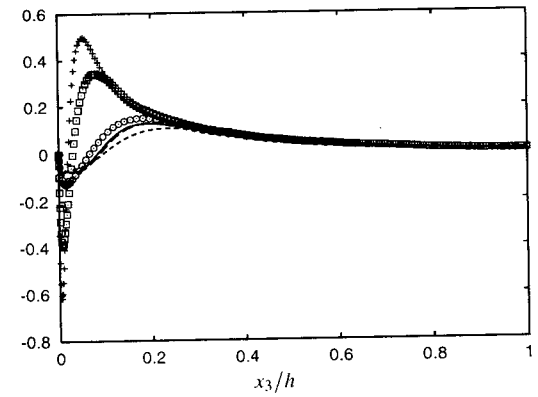

Figure 11: Π_{33} normalized by $u_{av}\tau_w/h$. *Compressible cases*: ——, $Re_\tau = 545$, $Ma = 3$; – – –, $Re_\tau = 455$, $Ma = 2.5$; - - - -, $Re_\tau = 221$, $Ma = 1.5$. *Incompressible cases* (Moser, 1999): ⊙ $Re_\tau = 180$; □ $Re_\tau = 395$; + $Re_\tau = 590$.

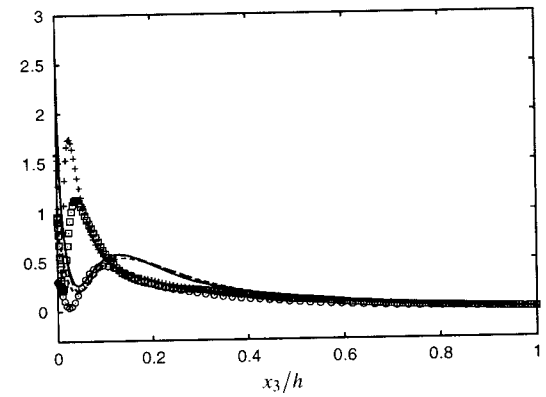

Figure 12: Π_{13} normalized by $u_{av}\tau_w/h$. *Compressible cases*: ——, $Re_\tau = 545$, $Ma = 3$; – – –, $Re_\tau = 455$, $Ma = 2.5$; - - - -, $Re_\tau = 221$, $Ma = 1.5$; · · · · · ·, $Re_\tau = 181$, $Ma = 0.3$. *Incompressible cases* (Moser, 1999): ⊙ $Re_\tau = 180$; □ $Re_\tau = 395$; + $Re_\tau = 590$.